Review of Scientific Instruments

RESEARCH ARTICLE | AUGUST 02 2024

Design solutions for the hodoscope of the magnetic proton recoil neutron spectrometer of the SPARC tokamak

Special Collection: Proceedings of the 25th Topical Conference on High-Temperature Plasma Diagnostics

M. Dalla Rosa ; S. Mackie ; D. Rigamonti ; L. G. Tedoldi; S. Colombi ; A. Dal Molin ; G. Marcer ; M. Nocente ; G. Gorini ; P. Raj ; M. Rebai ; J. Carmichael ; M. Reinke ; F. Scioscioli ; R. A. Tinguely ; M. Tardocchi

Check for updates

Rev. Sci. Instrum. 95, 083508 (2024)
https://doi.org/10.1063/5.0219463

View Online Export Citation

Articles You May Be Interested In

Ion optical design of the magnetic proton recoil neutron spectrometer for the SPARC tokamak

Rev. Sci. Instrum. (October 2024)

Overview of the neutron diagnostic systems for the SPARC tokamak

Rev. Sci. Instrum. (October 2024)

Development of a bolometry diagnostic for SPARC

Rev. Sci. Instrum. (August 2024)

30 June 2025 15:31:08

AIP Publishing

Special Topics Open for Submissions

Learn More

AIP Publishing

Review of Scientific Instruments ARTICLE pubs.aip.org/aip/rsi

Design solutions for the hodoscope of the magnetic proton recoil neutron spectrometer of the SPARC tokamak

Cite as: Rev. Sci. Instrum. 95, 083508 (2024); doi: 10.1063/5.0219463
Submitted: 17 May 2024 • Accepted: 1 July 2024 •
Published Online: 2 August 2024

View Online Export Citation CrossMark

M. Dalla Rosa,[1,a)] S. Mackie,[2] D. Rigamonti,[3] L. G. Tedoldi,[1] S. Colombi,[1] A. Dal Molin,[3] G. Marcer,[1] M. Nocente,[1] G. Gorini,[1] P. Raj,[4] M. Rebai,[3] J. Carmichael,[4] M. Reinke,[4] F. Scioscioli,[3] R. A. Tinguely,[2] and M. Tardocchi[3]

AFFILIATIONS

[1] Department of Physics, University of Milano-Bicocca, Milan 20126, Italy
[2] Plasma Science and Fusion Center, Massachusetts Institute of Technology, Cambridge, Massachusetts 02139, USA
[3] Institute for Plasma Science and Technology, National Research Council, Milan 20125, Italy
[4] Commonwealth Fusion Systems, Devens, Massachusetts 01434, USA

Note: This paper is part of the Special Topic on Proceedings of the 25th Topical Conference on High-Temperature Plasma Diagnostics.
[a)] **Author to whom correspondence should be addressed:** m.dallarosa@campus.unimib.it

ABSTRACT

A new 14 MeV neutron spectrometer utilizing the magnetic proton recoil (MPR) technique is under development for the SPARC tokamak. This instrument measures neutrons by converting them into protons, whose momenta are subsequently analyzed using a series of magnets before detection by an array of scintillators known as the hodoscope. In this work, we explore various solutions for the hodoscope detectors through laboratory tests with radioactive sources and simulations. We present findings on light collection and pulse shape discrimination based on detector types, as well as optimal solutions for photo-detectors studying the differences between SiPM and PMT. Our results also led to the determination of a better optimized design for the hodoscope detectors, consisting of a 0.7 cm width and a 13 cm length *EJ276D* scintillation rod.

© 2024 Author(s). All article content, except where otherwise noted, is licensed under a Creative Commons Attribution (CC BY) license (http://creativecommons.org/licenses/by/4.0/). https://doi.org/10.1063/5.0219463

30 June 2025 15:31:08

I. INTRODUCTION

The SPARC tokamak is a compact, high-field fusion device developed by Commonwealth Fusion Systems (CFS)[1] and under construction at Devens, MA (USA). It aims to demonstrate a net energy gain (Q-fus > 1) from fusion reactions, which is a crucial step toward practical fusion power generation. SPARC[2] utilizes rare-earth barium copper oxide (REBCO)[3] based high-temperature superconducting magnets to achieve strong magnetic fields of about $B_0 = 12.2T$, enabling more efficient confinement of the fusion plasma. This design is expected to lead to the development of smaller, more cost-effective fusion machines than those currently being built, such as ITER,[4] while still being capable of producing abundant, clean energy. To study the properties of the plasma, a neutron spectrometer[5] based on the Magnetic Proton Recoil (MPR) technique[6] is under development as a collaboration between CFS, the University of Milano Bicocca, the Institute for Plasma Science and Technology, National Research Council (ISTP-CNR), and the Massachusetts Institute of Technology (MIT). Neutron spectroscopy allows us to assess the ion temperature, the D/T ratio, and the thermal and non-thermal components of fusion power.[7–9] In order to design the MPR, the following aspects need to be carefully taken into account:

1. The neutrons need to be well collimated in order to preserve their direction before the elastic scattering (n, p) on a hydrogen-rich material, such as polyethylene.
2. Only the protons emitted at small angle collisions ($\theta \sim 0^\circ$) are selected and dispersed by a magnetic field,[10] which will

© Author(s) 2024

separate them depending on their momentum. The energy of the proton E_p follows this relationship:

$$E_p = E_n \cos^2(\theta), \tag{1}$$

where E_n is the neutron energy.

3. The momentum-sorted protons reach a set of detectors on the focal plane of the MPR, known as the hodoscope, designed to measure the spatial dispersion associated with their energy. The relationship between the energy E and the momentum p is

$$E = \frac{p^2}{2m}. \tag{2}$$

Due to its segmented structure, the hodoscope is able to cope with counting rates as high as 500 kHz. Each of the channels consists of a rod of scintillation material coupled via a light guide to a photosensor. In each channel, the number of protons that impinge is recorded. Subsequently, these data are utilized to generate a spatial histogram, effectively representing the energy spectrum of the detected protons.

Given the design of the MPR defined in Ref. 10, the energy region of interest spans about 40 cm. It is covered by 40 channels, which nominally have a width of 1 cm (see further below). Each stage of the magnetic proton recoil technique adds uncertainties to the energy resolution ΔE,

$$\Delta E^2 = \Delta E^2_{target} + \Delta E^2_{optic} + \Delta E^2_{hodoscope}. \tag{3}$$

In Eq. (3), ΔE^2_{target}, $\Delta E^2_{hodoscope}$, and ΔE^2_{optic} are the contributions linked to the processes that the protons undergo when they interact with specific elements on the MPR. ΔE^2_{target} is associated with the interaction at different positions of the neutron on the polyethylene target and the new-born protons energy loss inside the target due to charged particle interaction inside a material. ΔE^2_{optic} is associated with the dispersion that protons undergo in the different components of a MPR, such as the magnetic field, the collimators, and angle straggling. In this paper, different designs of a single channel of the hodoscope will be studied to minimize the contribution of $\Delta E^2_{hodoscope}$, for example, by optimizing the width and length of the scintillator rod. Two approaches are followed to determine the best configuration: an experimental one, in which different setups are used in the laboratory to change both the photosensor and scintillation material; and a computational one, in which the dimensions (length and width) of the scintillation rods are studied.

II. METHODS

Two organic scintillators, *EJ*200 and *EJ*276*D*, have been studied as possible solutions for the detectors of the hodoscope. They have similar performances in terms of scintillation decay time (around 10 ns) and light yield, but the *EJ*276*D* has pulse shape discrimination (PSD) capabilities associated with different decay times for different particles. Since the tokamak is a harsh environment characterized by a high neutron [order of 10^9 n/(s cm^2)] and comparable gamma-ray flux (due to, mostly, neutron activation and plasma nuclear reaction) in the central channel for the maximum power scenario, the opportunity to discriminate against the gamma-ray background is a crucial aspect for improving the signal-to-background ratio of the MPR. The scintillator rods used have the following dimensions: 1 × 1 × 11 cm^3. The choice comes from matching the proton dispersion capabilities of the magnets. Numerical simulations reveal that protons with energies in the range of 11–18 MeV will be dispersed over a 50 cm wide region. Taking into account the energy bite of the magnetic field and by choosing 1 cm wide detectors, the neutron energy histogram will be made of 40 channels covering the region, which is deemed sufficient for our scope (see further below). In this paper, optimizations on the depth of the scintillator were not made, and this dimension was chosen to match the width. In future studies, the depth of the scintillation rod will be studied, and we expect that for different regions, the depth will need to be varied to stop the proton interaction. The spread of protons in the direction perpendicular to the dispersion direction is the largest for the highest energy protons. As is shown later (see Fig. 6), for example, 18 MeV protons have a traverse spread of 11 cm ($\pm 2\sigma$). The scintillators are coupled to a photosensor to convert the scintillation light into an electrical signal. Historically, the most common photosensor has been the photomultiplier tube (PMT), which is based on a well-established technology. In the last few decades, an innovative device based on multiple avalanche photodiodes, namely, the Silicon Photomultiplier (SiPM), has been introduced. The latter is a compact device insensitive to magnetic fields (unlike unshielded PMTs). The performance of these two photosensors has been addressed in this paper. The output electric signal emitted by the photosensor has been fed into a DT5730 CAEN digitizer (500 MSps, 14 bits) able to perform online analysis of the signals. Pulse shape discrimination (PSD) analysis has also been carried out by comparing signals integrated over a long-gate corresponding to the full waveform and a short-gate corresponding to the fast decaying component of the waveform. Finally, a radioactive γ-(source^{137}Cs) and an α-(source^{241}Am) have been used to test the detectors. In Sec. III, different configurations are studied to identify the optimal choice. In Sec. IV, results from a Monte Carlo code[11] are presented to determine the proton distribution along the hodoscope in the dispersive (x) and perpendicular (y) directions. This framework describes where the protons were drifted by the magnetic fields impinging on the hodoscope. Finally, in the conclusion (IV), the main results will be outlined and discussed.

III. STUDY OF THE COMPONENTS

In this section, different tests performed to compare the various detector unit subparts and their configurations are outlined, and the results are discussed.

A. Coating choice

Preliminary tests were conducted to determine the most suitable light-tight coating solutions for the scintillation rods. Three distinct conditions were examined by acquiring a spectrum utilizing a PMT and the *EJ*276*D* rod: uncoated, aluminum foil-coated, and Teflon tape-coated. As expected, the uncoated condition yielded significantly diminished light collection (9%) due to scintillation photon loss compared to the aluminum case. While aluminum demonstrated a slightly lower light collection efficiency (90%) compared to Teflon tape, its practical manufacturability rendered it the

30 June 2025 15:31:08

© Author(s) 2024

preferred choice for subsequent experiments. Therefore, all tests detailed in Sec. III B utilized aluminum coating.

B. Scintillators and photosensors choice

Multiple experiments were conducted to determine the optimal detector configuration concerning scintillator materials and photosensor selections.

1. Scintillation material

Two tests were performed to assess the properties of the scintillation rods. The light yield was evaluated by acquiring spectra with both rods coupled to a PMT and operated at 900 V. *EJ*200 demonstrated a higher scintillation efficiency of 40% compared to *EJ*276*D* with a γ-source in this set-up at the same bias voltage.

2. Pulse shape discrimination capabilities

A noteworthy feature of *EJ*276*D* is its capability for PSD. When ionizing radiation interacts with the scintillation material, the lattice of the plastic scintillator undergoes excitation. Depending on the nature of the interacting radiation, varying de-excitation times occur due to quenching effects. Consequently, there can be different, particle dependent time intervals during which scintillation photons are emitted and subsequently collected. This PSD capability is illustrated in Fig. 1, which is a 2D graph of the PSD parameter against the digitizer channel number. Here, the PSD parameter is defined as

$$PSD = \frac{Q_{long} - Q_{short}}{Q_{long}}. \tag{4}$$

Here, Q_{long} represents the charge collected in a time window long enough to contain the entire waveform [250 ns], and Q_{short} represents the charge collected in a smaller time window [38 ns]. These values were empirically chosen. These data come from a PMT spectrum. The colors on the graph depict the local density of events expressed in arbitrary units using a Python script. In our test, we irradiated the detector with a ^{137}Cs γ-ray and a ^{241}Am α-particle emitter. Hence, we expect a different pulse shape depending on the radiation type. Four different regions can be seen in the figure. The gamma-ray region and the alpha-particle region are near each other, and a line positioned at PSD = 0.366 separates them. This line was empirically chosen to visualize the difference between these two regions. However, from this preliminary analysis, the two regions still overlap. In future tests, we expect to see a clearer division between the gamma-ray region and the proton particle region through Q-long and Q-short optimization. In the upper part of the graph, a third population of piled-up waveforms can be seen. In this region, two or more waveforms were recorded by the photosensor within an acquisition record. A fourth region around channel 50, with a PSD value between 0.15 and 0.35, depicts low energy x-rays. A clear difference between the gamma and alpha populations can be seen, making the *EJ*276*D* a viable solution to effectively remove the gamma-ray background to increase the signal-to-background ratio.

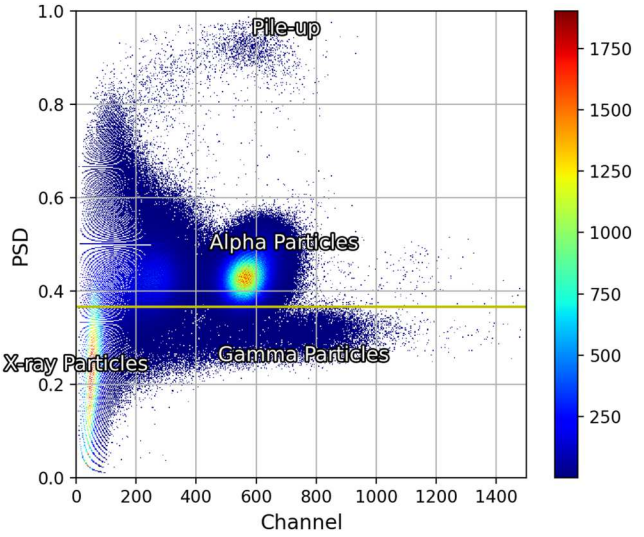

FIG. 1. Figure of merit of PSD plotted against the pulse height channel with Eq. (3). The line at PSD = 0.366 indicates the cut chosen to separate alpha and gamma particles.

3. Photosensors

Two photosensors underwent testing to evaluate their time responses. To visualize this effect, different waveforms with a given PSD parameter and energy were sampled from Fig. 1 for both a PMT and a SiPM and then averaged. The difference is evident in Fig. 2. The PMT outpaced the SiPM by a time-factor of 3. This parameter was calculated as the ratio of the time intervals in which the signal for each photosensor starts to rise and the time at which the signal reaches 20% of the maximum signal during the fall phase,

$$ratio = \frac{SiPM[t_{20\%signal} - t_{start}]}{PMT[t_{20\%signal} - t_{start}]}. \tag{5}$$

This difference arises from the intrinsic characteristics of each photosensor type: in PMTs, incident photons prompt the emission of electrons, which undergo amplification via a series of dynodes to generate an amplified output signal. Conversely, SiPMs rely on the generation of electron–hole pairs in a silicon semiconductor by incident photons, followed by charge multiplication through avalanche breakdown. Regarding the speed of these two photosensors, the generation of a signal in the dynode chain of a PMT is much faster than the charge collection in a silicon detector. Moreover, PMTs exhibit lower intrinsic capacitance compared to SiPMs, further contributing to their higher speed.

C. Light guide analysis

In a hodoscope, multiple detectors are simultaneously operated, with the scintillation rods side by side. It is useful to know how the displacement of the photosensor due to a light guide affects the measurement. This consideration arises because photosensors are typically larger than scintillation rods, preventing them from being placed side by side. In this setup, the scintillation rod base (1.0 × 1.0 cm^2) is coupled to one side of the light guide composed of Poly(methyl methacrylate), also known as PMMA, with dimension 1.0 × 1.0 cm^2 to capture all emitted light. The light guide is 1 cm

30 June 2025 15:31:08

© Author(s) 2024

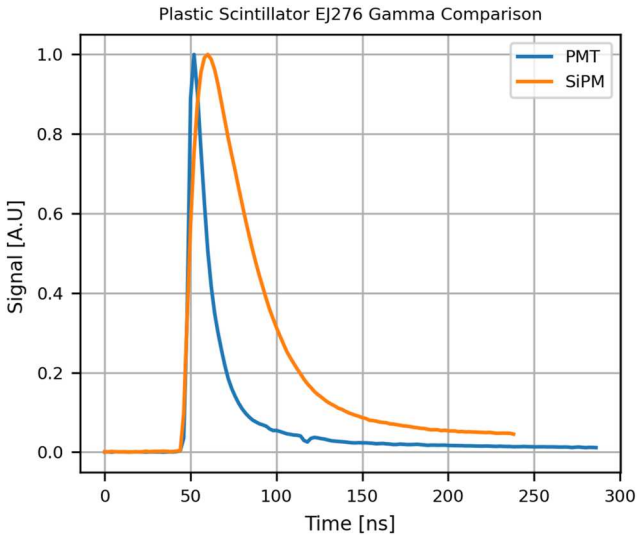

FIG. 2. Comparison of two normalized gamma pulses captured by two distinct photosensors (PMT, blue curve; and SiPM, orange curve).

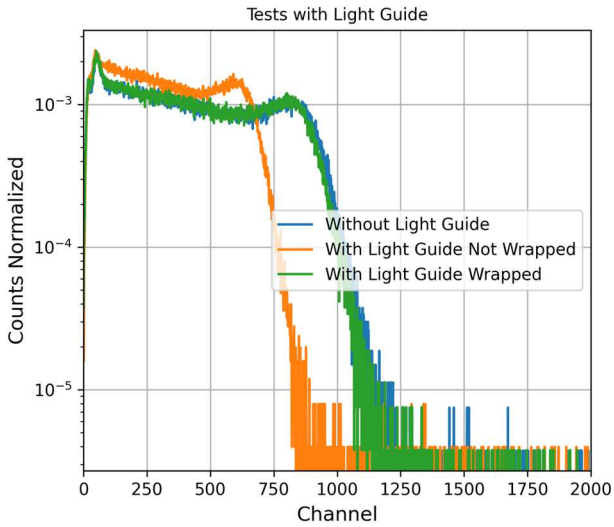

FIG. 3. Effect of different light guide options on the pulse height spectrum collected by the hodoscope detector when irradiated with a γ-source.

long, and it transforms a quadratic (1 cm square side) cross section area into a circular one. The opposite side of the light guide (1.0 cm diameter) is connected to a photosensor (PMT with a photocathode of 3, 8 cm diameter), with both couplings made using optical grease. To assess potential light loss, three spectra were acquired under the following conditions:

1. Scintillator rod wrapped in aluminum foil coupled with optical grease to a photosensor: this configuration yields the best light collection.
2. Scintillator rod wrapped in aluminum foil, coupled with an uncoated light guide, and connected to a photosensor: This configuration resulted in light loss.
3. Scintillator rod wrapped in aluminum foil coupled alongside a light guide and connected to a photosensor: This configuration yielded the same light collection as configuration 1.

The light collected in configurations 1 and 3 was found to be quantitatively identical. Based on this result, displacing the photosensor with wrapped light guides is a viable and effective solution. This analysis can be seen in Fig. 3, where the three different conditions are depicted. In the second condition, the light collection is reduced by 25%.

D. Study of the positions of interactions

In a magnetic proton recoil, given the geometry of the magnet, protons are momentum separated and interact on the hodoscope in different positions. The position of interaction along the x-axis gives information about the proton-energy. Due to different aspects, such as the collision on the polyethylene target and the original direction of the neutron, protons are also spread along the y-axis. The protons, which interact in different positions along the bar (y-axis), generate scintillation photons at different positions. The signal collected at the photosensor side can, therefore, vary between protons that have interacted near the photosensor and those far away from it. This is because the light transport inside the scintillator from the position of impact to the photosensor is not ideal, and some light can be lost along its path to the photosensor. To assess this aspect, holes were suitably made in the aluminum coating at various

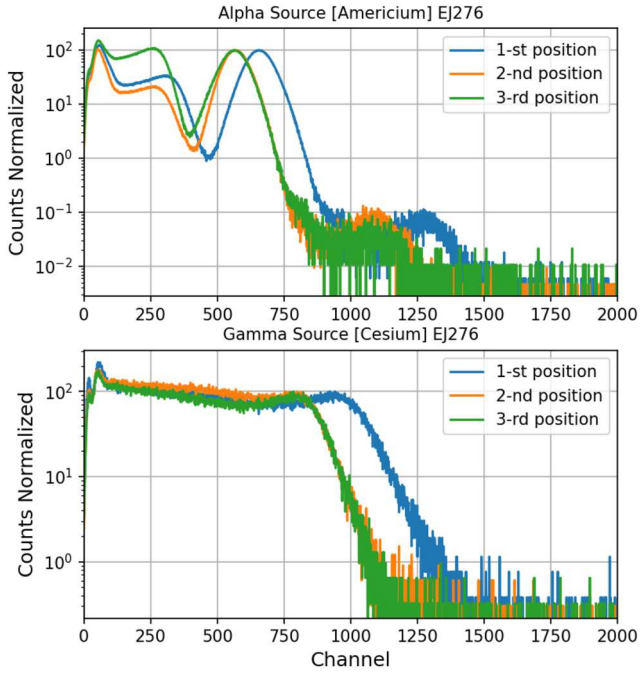

FIG. 4. Illustration of the different positions of the interaction of α-source and γ-source using a PMT along the 11.0 cm scintillation rod. The difference in the amount of light collected as a function of traveling path length can be appreciated.

30 June 2025 15:31:08

© Author(s) 2024

positions, corresponding to different fractions of the rod's length: a quarter (first position), half (second position), and three quarters (third position). In this configuration, the photosensor was coupled to the scintillation rod on the square side, near the first position. Subsequently, γ-source and α-source were positioned over the respective holes to simulate interactions at different positions along the scintillation rod. Analysis in Fig. 4 indicates considerable variance in light collection between the first and second holes, while consistency is observed between the second and third holes. In particular, *EJ276D* exhibited a 12% light collection loss, whereas *EJ*200 experienced a 7% decrease when comparing the first and second holes. This can be an issue since the protons will be impinging on the entire scintillation surface. To address this issue, the scintillation rod was paired with a photosensor (2 PMTs) on each side. This configuration resulted in uniform light collection across the rod. This systematic approach clarifies the impact of interaction position on signal variation and underscores the efficacy of employing dual photosensors to mitigate light collection differences along the scintillation rod.

IV. STUDY OF THE SCINTILLATOR ROD DIMENSION

Utilizing the Monte Carlo method, two distinct studies were conducted to investigate the width and length of the scintillation rod.

A. Width of the scintillator

In a magnetic proton recoil, each channel of the hodoscope corresponds to a specific energy range. To optimize light collection and energy resolution, simulations were conducted using the Monte Carlo method. A beam of protons with a prescribed energy distribution was simulated, and a magnetic field[10] was used to drift the protons along the x-and y-axes.[11] The x-axis was then calibrated in energy, allowing for the generation of a histogram with adjustable bin widths. The simulated energy distribution represents the broadening of a DT peak with an ion temperature Ti of 10 keV. Several simulations were performed, varying the bin size from 1 to 10 mm. The parameter of interest is the number of bins that cover the full width at half maximum (FWHM). This parameter matters since it is important to have enough channels to have sufficient energy resolution. In Fig. 5, a bin width of 7 mm is depicted, revealing that the FWHM of the energy distribution (4 cm–560 keV) is covered by six bins. From the previous simulations, the FWHM with a bin size of 1 cm is covered by four bins. Based on these results, it is evident that reducing the detector width from 1.0 to 0.7 cm would lead to an improved, more resolved measurement. In an ideal situation, having the smallest bin size possible would lead to better resolution, but this choice must be weighted both on the cost and the statistics: having more scintillators means having a denser hodoscope, and the costs would increase. There is also a second side associated with the fact that having more bins means that enough protons should impinge on the bin to have good statistics. The 7 mm size is a good trade-off between these characteristics. These simulations were done without taking into account the target contributions or the loss of energy the protons experience inside the target.

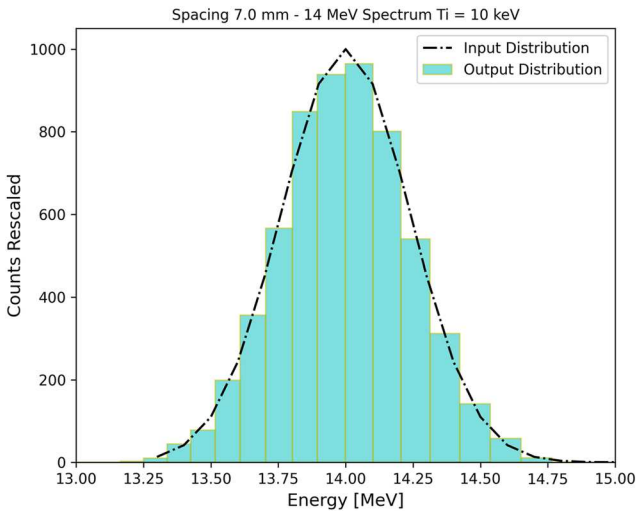

FIG. 5. Simulation depicting the broadening of a DT peak with a Ti of 10 keV. It is observed that the FWHM is spanned by six bins of size 0.7 cm. The dotted line represents the input distribution; the output distribution is evaluated by the position of interaction on the different bins. Each bin position is then energy calibrated. The target contribution is not taken into account.

B. Length of the scintillation

It is crucial to evaluate the number of particles that may fall outside the hodoscope due to the insufficient length of the scintillation rod. To gain insight into this, simulations of different mono-energetic rays were conducted, and their interactions were studied along the y-axis.

In Fig. 6, the dispersion along both the x-axis and y-axis is illustrated with mono-energetic rays from 10 to 20 MeV. With a scintillation rod length of 11 cm, for the 17 MeV mono-energetic ray, certain protons within the intervals $[-3\sigma, -2\sigma]$ and $[2\sigma, 3\sigma]$ end up outside the hodoscope. Here, σ represents the standard deviation of the mono-energetic ray across the y-axis. By increasing the length of the scintillation rod to 13 cm, all protons would be contained within the hodoscope. An alternative solution to mitigate information loss

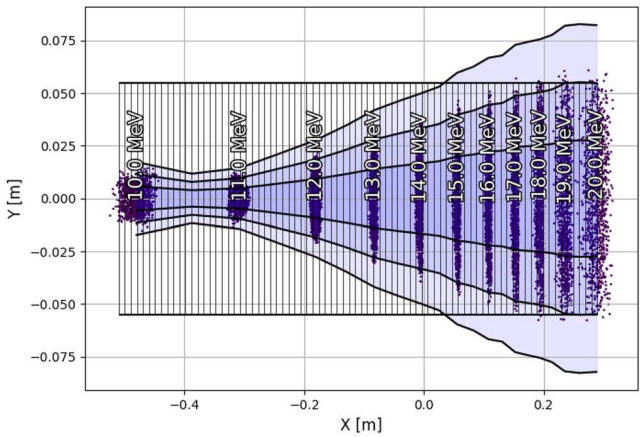

FIG. 6. Distributions of protons positions on a hodoscope with 11 cm long rods. 11 different energies in the interval 10–20 MeV were simulated. The blue bands (dark to light) indicate $\pm1\sigma$, $\pm2\sigma$, and $\pm3\sigma$ bounds of the resulting proton intensity distributions.

30 June 2025 15:31:08

© Author(s) 2024

could involve estimating the percentage of protons that miss the hodoscope and are present in the different σ intervals and correcting for this value accordingly.

V. CONCLUSIONS

In this paper, several tests were conducted to assess the performances of different experimental setups in support of the design of detectors for the hodoscope of the SPARC MPR neutron spectrometer. The initial test aimed to determine the optimal coating, with aluminum emerging as the preferred choice. Despite exhibiting a lower light yield compared to the *EJ*200, the *EJ*276*D* demonstrated promising results due to its pulse shape discrimination capability. In addition, PMTs exhibited faster time responses than SiPMs, enabling operation at higher rates. Moreover, the presence of a light guide did not significantly diminish light collection. The position of proton interaction on the scintillation rod emerged as a potential challenge, which was addressed by employing two photosensors on both ends of the rod. Computational simulations were utilized to investigate the width and length of the rod. From the information collected through this analysis, it was found that, from the initial rod design of $1.0 \times 1.0 \times 11.0$ cm^3 increasing the length from 11.0 to 13.0 cm, and reducing the width from 1.0 to 0.7 cm could help to collect all the protons and improve the energy resolution. The present solutions are ideal, but they will need further optimization from the perspectives of manufacturability, cost, and, most importantly, engineering compatibility with the MPR vacuum and clean environments.

ACKNOWLEDGMENTS

This work was supported by Commonwealth Fusion Systems and ENI SpA.

AUTHOR DECLARATIONS

Conflict of Interest

The authors have no conflicts to disclose.

Author Contributions

M. Dalla Rosa: Conceptualization (equal); Data curation (equal); Formal analysis (equal); Investigation (lead); Methodology (equal); Software (equal); Supervision (equal); Validation (equal); Visualization (equal); Writing – original draft (lead); Writing – review & editing (lead). **S. Mackie**: Investigation (equal); Methodology (equal); Software (equal); Validation (equal). **D. Rigamonti**: Conceptualization (equal); Data curation (equal); Investigation (equal); Methodology (equal); Supervision (equal); Validation (equal). **L. G. Tedoldi**: Conceptualization (equal); Data curation (equal); Formal analysis (equal); Investigation (equal); Methodology (equal); Software (equal); Validation (equal); Visualization (equal). **S. Colombi**: Investigation (equal). **A. Dal Molin**: Investigation (equal); Software (equal); Supervision (equal); Validation (equal). **G. Marcer**: Investigation (equal). **M. Nocente**: Conceptualization (equal); Data curation (equal); Investigation (equal); Supervision (equal); Validation (equal). **G. Gorini**: Conceptualization (equal); Project administration (equal); Resources (equal); Supervision (equal). **P. Raj**: Investigation (equal); Project administration (equal); Supervision (equal). **M. Rebai**: Investigation (equal); Methodology (equal); Visualization (equal). **J. Carmichael**: Investigation (equal). **M. Reinke**: Investigation (equal); Project administration (equal); Resources (equal); Supervision (equal). **F. Scioscioli**: Conceptualization (equal); Investigation (equal); Validation (equal). **R. A. Tinguely**: Investigation (equal); Supervision (equal). **M. Tardocchi**: Funding acquisition (equal); Investigation (equal); Project administration (equal); Resources (equal); Supervision (equal); Visualization (equal).

DATA AVAILABILITY

The data that support the findings of this study are available from the corresponding author upon reasonable request.

REFERENCES

[1] See https://cfs.energy for CFS site.
[2] A. J. Creely *et al.*,"Overview of the SPARC tokamak," J. Plasma Phys. **86**, 865860502 (2020).
[3] D. G. Whyte *et al.*, "Experimental assessment and model validation of the SPARC toroidal field model coil," IEEE Trans. Appl. Supercond. **34**(2), 0600218 (2024).
[4] F. Romanelli *et al.*, Fusion electricity: A roadmap to the realisation of fusion energy (2012).
[5] P. Raj *et al.*, "Overview of the preliminary design of SPARC's neutron diagnostic systems" (2024) (these proceeding).
[6] E. Andersson Sundén *et al.*,"The thin-foil magnetic proton recoil neutron spectrometer MPRU at jet," Nucl. Instrum. Methods Phys. Res., Sect. A **610**, 682–699 (2009).
[7] D. Rigamonti *et al.*,"The single crystal diamond-based diagnostic suite of the JET tokamak for 14 MeV neutron counting and spectroscopy measurements in DT plasmas," Nucl. Fusion **64**, 016016 (2024).
[8] M. Nocente *et al.*, Rev. Sci. Instrum. **93**, 093520 (2022).
[9] J. Eriksson *et al.*,"Measuring fast ions in fusion plasmas with neutron diagnostics at JET," Plasma Phys. Controlled Fusion **61**, 014027 (2019).
[10] S. Mackie, Ion optical design of NSPC, the magnetic proton recoil neutron spectrometer for burning plasma diagnosis of the SPARC tokamak (2024).
[11] See https://github.com/shonmackie/MPR_Tools for Mpr_tools repository.

30 June 2025 15:31:08

© Author(s) 2024